CHAPTER 1

INTRODUCTION

This chapter starts with the development history of the surface plasmons, surface plasmon polaritons (SPPs), and spoof surface plasmon polaritons (SSPPs). First, a brief review of the theoretical and experimental study of the surface plasmons has been discussed. Then, the fundamental characteristics of surface plasmon polaritons (SPPs) and spoof surface plasmon polaritons (SSPPs) are discussed. After that, this chapter briefly summarized the various SSPPs-based devices, including SSPPs waveguides, filters, couplers, power splitters, leaky wave antennas, and endfire antennas. Further, this chapter covers the MIMO system and different sources of mutual coupling in its implementation. MIMO system performance metrics are also discussed, which will ensure its proper functioning. Later, reflectarray system design, challenges, and operational principles are discussed. Finally, a motivation to implement the SSPPs concept in various applications is presented in this chapter.

1.1 Surface Plasmons

The self-sustained collective excitations at metal surfaces are the typical energy losses of fast electrons flowing through thin metal films investigated by Ritchie in his groundbreaking study [1]. Additionally, he looked at how film boundaries affected the production of collective excitations and discovered that the boundary effect results in the appearance of a new, decreased loss because surface collective oscillations are excited. Two years later, Powell and Swan [1, 2] demonstrated the presence of these collective excitations in a series of electron energy-loss experiments; Stern and Ferrell termed the quanta of these excitations the surface plasmons (SPs) [3].

The theoretical and experimental studies of surface plasmons (SPs) have advanced significantly since then. Surface plasmons (SPs) are employed in various fields like electrochemistry [4], biosensing [5,6], scanning tunneling microscopy [7], and surface-plasmon microscopy [8,9]. The most attractive aspect of these surface plasmons (SPs) is their use to concentrate light in subwavelength structures and enhance transmission through periodic arrays of subwavelength holes in optically thick metallic films [10]. SPs can also be used as a foundation for subwavelength waveguide component design, manufacture, and characteristics [11–18]. SPs originally existed at optical frequencies. SPs are the highly localized modes at the surface of two materials of opposite signs (*i.e.*, metal-dielectric interface) in the real parts of the permittivities [19].

SPs can be considered as the limiting case of surface plasmon polaritons (SPPs) when the speed of light is allowed to become infinitely large. They are computed from solutions of Laplace's equation for a scalar potential whose amplitudes decay exponentially with increasing distance from the interface into each medium and which propagate along a planar metal-dielectric interface in a wavelike manner. Consequently, they are surface waves that are electrostatic. They may be associated with non-propagating collective vibrations of the electron plasma close to the metal surface [20].

1.2 Surface Plasmon Polaritons (SPPs)

Surface plasmon polaritons (SPPs) are unique surface waves that exist at the metal (a conductive material) and dielectric (a non-conductive material) interface in the optical regime. The interaction between the incident wave's electromagnetic (EM) field and the electrons plasma close to the metal surface causes collective oscillations to propagate along the interface. The strong interaction makes the electromagnetic field tightly restricted to the interface. Because of the highly conductive metal, the electric field must have a component that is perpendicular to the interface [19,21,22]. This behavior of the electromagnetic field at a metal-dielectric interface is shown in Fig. 1.1a. The SPP waves propagates along the x- direction and exponentially diminish in the direction perpendicular to the interface. They are transverse magnetic in nature (H is in the y-direction). The decay length of the field in the dielectric medium is δ_d, nearly half the wavelength of light involved, whereas the skin depth controls the decay length, δ_m, into the metal as depicted in Fig. 1.1b.

By applying Maxwell's equations, in the upper ($z > 0$) region, the magnetic and electric fields are discussed in [23] and written as,

$$H^+ = (0, A, 0)e^{-j\beta x - \alpha_1 z + j\omega t} \tag{1.1}$$

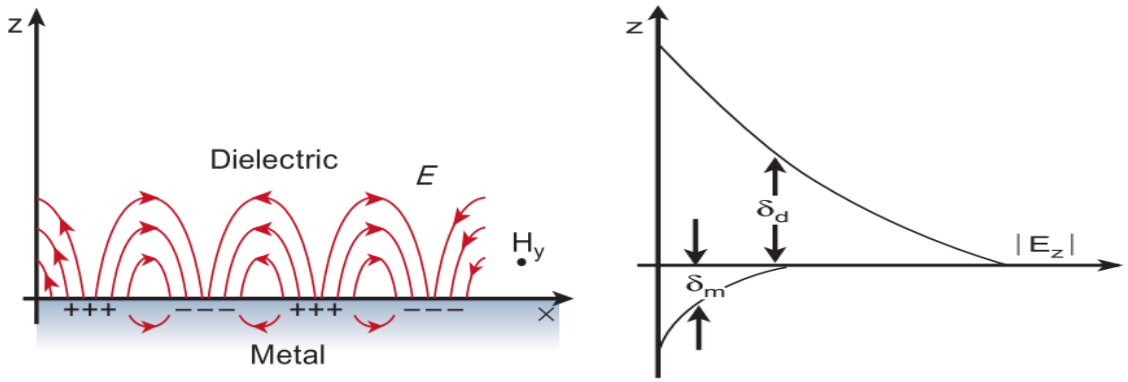

(a) (b)

Figure 1.1: (a) The EM field at the interface between a metal and a dielectric, and (b) the decay length in the dielectric and metal [19].

$$E^{+} = (-jk_1, 0, \beta)\frac{A}{\omega\varepsilon_1}e^{-j\beta x+\alpha_1 z+j\omega t} \tag{1.2}$$

In the lower ($z < 0$) region, they are given as

$$H^{-} = (0, B, 0)e^{-j\beta x+\alpha_2 z+j\omega t} \tag{1.3}$$

$$E^{+} = (-jk_2, 0, \beta)\frac{B}{\omega\varepsilon_2}e^{-j\beta x+\alpha_2 z+j\omega t} \tag{1.4}$$

where, $\beta = k_x$ is the x-directional wave vector, and the decay factors α_1 and α_2 are calculated as

$$\alpha_1 = \sqrt{\beta^2 - \epsilon_1(\omega/c)^2} \tag{1.5}$$

$$\alpha_2 = \sqrt{\beta^2 - \epsilon_2(\omega)(\omega/c)^2} \tag{1.6}$$

The complex analysis of electromagnetic waves is done using the notation $j = \sqrt{-1}$. To confirm the strong field confinement of the electromagnetic waves, the E and H fields in Equations (1.1)-(1.4) should diminish exponentially, and resulting, Re (α_1) and Re (α_2) should be positive. Applying an appropriate boundary condition ensures that the E and H fields' transverse components are continuous at the interface; the surface-plasmon condition is as follows, as given [23] below,

$$\frac{\alpha_2}{\alpha_1} = -\frac{\epsilon_2(\omega)}{\epsilon_1} \tag{1.7}$$

Equation (1.7) indicates that ϵ_2 should be negative because the SPPs are localized to the interface. Indeed, according to the Drude-Lorentz model, a dielectric function that is frequency-dependent with $\epsilon_2(\omega) = \epsilon(\omega)$- j$\epsilon(\omega)$, and as a result, it has a negative real component below its inherent plasma frequency, which primarily lies in the range of the UV spectrum. Factually, SPPs typically occur at frequencies lower than UV. By using the relationship given in Equations (1.5), (1.6), and (1.7), the dispersive wave number for the SPPs can be determined as

$$\beta = k_0\sqrt{\frac{\epsilon_1\epsilon_2(\omega)}{\epsilon_1 + \epsilon_2(\omega)}} \tag{1.8}$$

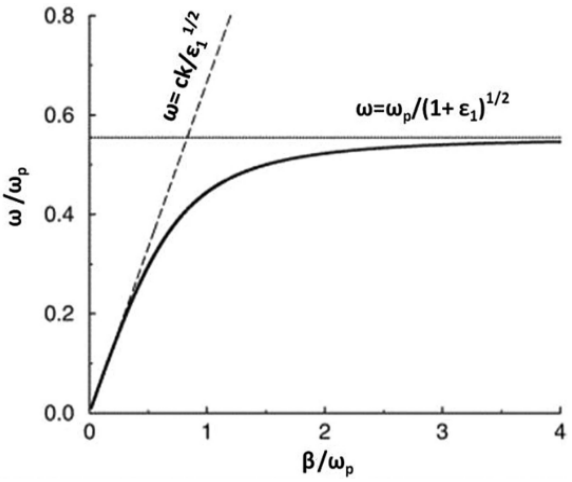

Figure 1.2: Dispersion curve of SPPs at the metal-dielectric interface [20].

The standard dispersion relation given in equation (1.8) for the SPPs at the interface between the metal without damping and the dielectric with permittivity ϵ_1 is shown in Fig. 1.2 [20]. The dotted line represents the light line that belongs to the plane waves in the dielectric medium. In contrast, the solid vertical line represents the classic nondispersive surface-plasmon frequency, $\omega = \omega_p/(1+\epsilon_1)^{1/2}$. Fig. 1.2 pointed out two significant characteristics of SPPs. First, the SPPs waves are slow in nature since their dispersion curve is consistently located to the right of the light line, with a propagation constant greater than the waves in free space. However, the propagation constant drops near the low frequencies, and the interface's high confinement disappears. Therefore, the highly localized SPPs occur near the surface plasmon frequency. Second, the SPPs propagate along the interface at the same speed as the light wave group velocity. They start at zero frequency, gradually slow as the frequency increases, and become asymptotically confined as they reach the surface plasmon frequency.

These characteristics give the SPPs waves distinctive merits.
First, free space incident waves striking a smooth contact cannot generate SPP waves because of wave-vector mismatch since the SPP wave propagation constant is always greater than the free space plane waves. Second, an SPP wave has a smaller wavelength than the free space wave, and when it gets closer to the surface-plasmon frequency of ω, it reaches zero.

1.3 Spoof Surface Plasmon Polaritons (SSPPs)

Surface plasmon polaritons (SPPs) lose their features when the frequency is reduced to the lower frequency regions of terahertz (THz) and microwave domains because the metals behave more like good conductors than the electric plasmas with negative permittivity. In 2004, Pendry *et al.* analytically demonstrated that plasmonic metamaterials (spoof or engineered SPPs) could accomplish SPPs at low frequencies [24]. The metallic block that makes up the structure has a 2-D periodic configuration of square holes that comprise the structure with a dimension of $(a \times a)$ and a separation of (d), where a and d are significantly less than the wavelength. Creating a subwavelength square hole array in a metallic layer structure provides a way to generate an SPP-like mode and obtain negative permittivity for artificial metamaterials. Fig. 1.3a illustrates the details of the 3-D spoof SPPs structure. The incident wave stimulates the TE_{10} mode in the 3-D holes (which acts as square waveguides). Electromagnetic waves cannot propagate if the operating frequency is below the cut-off frequency of these waveguides. However, the electromagnetic fields decline exponentially along the z-axis, maintaining high field confinement akin to natural surface plasmon polaritons. Additionally, Fig. 1.3b displays a dispersion curve that resembles an SPPs, with the waveguide mode's cut-off frequency serving as the asymptotic frequency. Using an analytical method, Pendry *et al.* demonstrated in [24] that the modes' dispersion behavior near the perforated metallic layer resembles that of a natural surface plasmon:

$$k_{\parallel}^2 c_0^2 = \omega^2 + \frac{1}{\omega_p^2 - \omega^2} - \frac{64^4 a^4 \omega^4}{\pi^4 d^4} \tag{1.9}$$

where $k_{\parallel}$ is the transverse wavenumber, ω_p plasma frequency, c_0 is the speed of light in a vacuum. The light line can estimate the surface wavenumber at lower frequencies. The wavenumber approaches infinity when the frequency ω approaches ω_p. ω_p is the

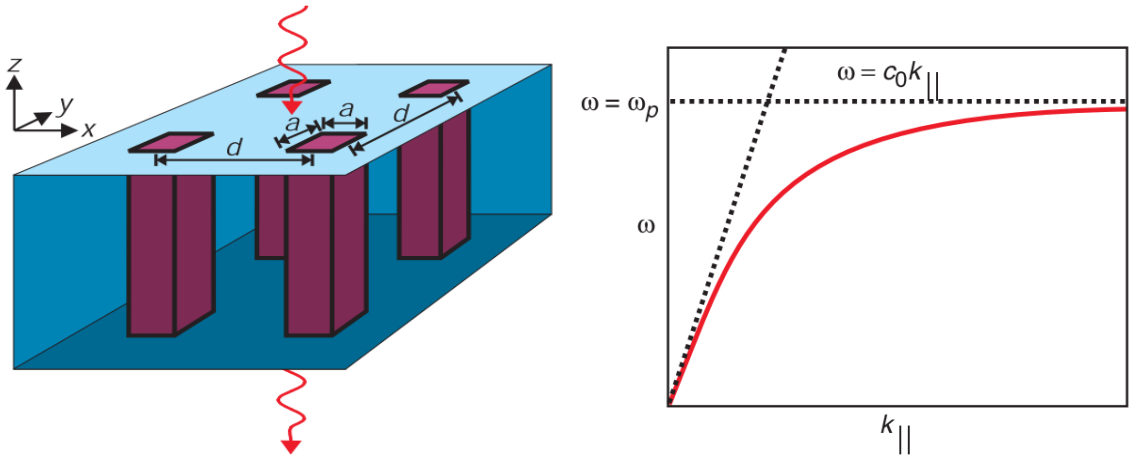

(a) (b)

Figure 1.3: (a) The 3-D structure to implement the Spoof SPPs, and (b) spoof surface plasmon dispersion relation on a structural surface [24].

plasmon frequency and is given [24] below:

$$\omega_p = \frac{\pi c_0}{1\sqrt{\epsilon_h \mu_h}} \tag{1.10}$$

where ϵ_h and μ_h are the hole's permittivity and permeability, respectively. After that, many spoof SPP structures were developed and theoretically and experimentally demonstrated SSPs-like mode. Hibbins *et al.* designed an artificial SPPs structure, which included a perforated metal layer. This experiment revealed that it supports SPP-like modes [25]. In [26], Shen *et al.* fabricated the planar U-shaped unit cell based structure on a ultrathin and flexible dielectric material to transfer the SSP modes. They demonstrated that even in cases where the SSP unit cells follow a curved trajectory, the field still propagates via their structures. Various structural surfaces that facilitate the propagation of SSPPs in terahertz and microwave frequency zones have been studied and reported in the literature [27–32], with the exception of the metallic surface depicted in Fig. 1.3a. An assortment of some of these contributions is shown in Fig. 1.4 (a-d).

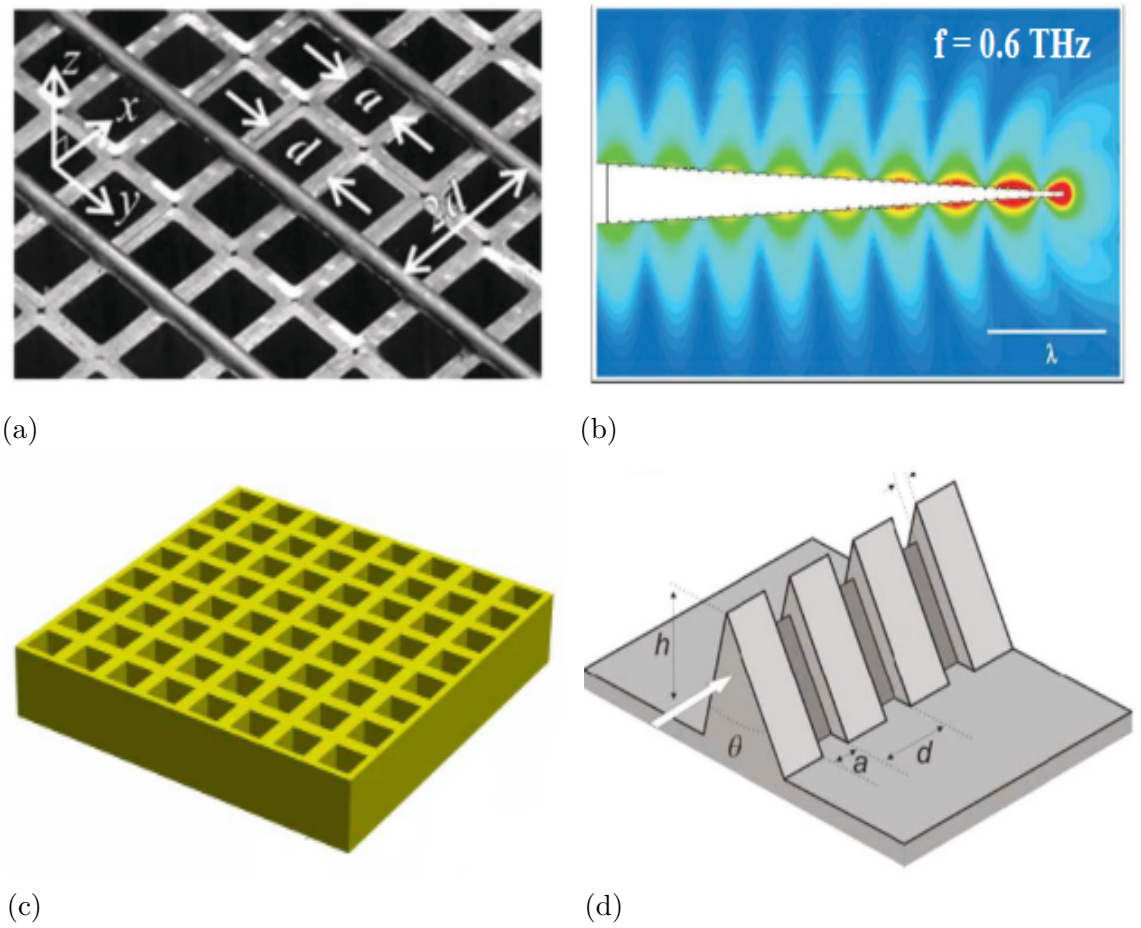

Figure 1.4: A set of spoof SPPs structures (a) the experimental sample shows the square brass tubes and cylindrical rods [25], (b) E-field superfocusing on a corrugated cone [27], (c) a square lattice of square holes [30], and (d) metallic wedge with a recurring pattern of grooves [31].

1.4 SSPPs-based Devices

Most contemporary microwave circuits and systems are built on high-integrated components and antennas. The rapidly increasing demand of the modern era for advanced systems simultaneously delivers high performance and compact size. However, signal integrity, interference suppression, and miniaturization are typically the three main hurdles in system design. Unfortunately, these aspects are nearly antagonistic. It can be observed in traditional microwave transmission lines (TLs), including the microstrip line (ML) and the coplanar waveguide (CPW), that placing adjacent lines closer to one another will unavoidably result in more cross-talk. At the same time, a corresponding loss of signal integrity will occur.

It has been shown both theoretically and experimentally that spoof SPPs exhibit the qualities of natural SPPs and offer novel approaches to the aforementioned problems. SSPPs-based waveguides have less cross-talk. Numerous spoof SPP waveguides, both bulky and planar, have been engineered in the microwave domain [26, 33–38]. Fig. 1.5 shows the few SSPPs based waveguide structures.

In [37, 38] Kianinejad *et al.* designed and modeled the slow-wave spoof surface plasmon modes-based TL and demonstrated the high isolation, as depicted in Fig. 1.5. Also, numerous passive SPP components and devices were developed, including filters [39–46], power dividers [34, 47, 48], couplers [26, 49], SPP rejection [50–52], demultiplexers [53, 54] etc. In [45], a novel broadband X-band BPF based on SSPPs in the microwave frequency band has been proposed using a coupled structure, as shown in Fig. 1.6. Jaiswal *et al.* designed the bandwidth (BW) reconfigurable BPF using spoof SPPs at THz/microwave frequency in [44, 46], as illustrated in Fig. 1.7. The H-shaped unit cell structure composite at the input and simple at the output have been used to ensure the impedance and wave vector matching. An UWB surface plasmonic Y-splitter is shown in Fig. 1.8a. Another frequency splitter was reported in [55], as depicted in Fig. 1.8b. A double-periodic grating spoof SPP TL is developed to obtain two SPP modes with distinct asymptotic frequencies. Two single periodic gratings with varying groove depths are used to build two branches at the output side that diverge at a 60° angle. This way, two SPP waves are divided into two branches in different frequency ranges.

The active SPP components and circuit design are crucial for practical applications. Zhang *et al.* proposed an effective amplification of SPPs in [56], as illustrated in Fig. 1.9. Amplifiers are often used to boost the SNR when weak signals are received from antennas or transmitted into space.

The SSPPs waves can also be converted into radiating waves by using plasmonic emitters known as antennas [57–62]. In [59], a 1-D phase-gradient metasurface and a corrugated metallic strip-based structure has been proposed to convert the SSPPs waves into spatially radiating waves, as shown in Fig.1.10. The SSPPs waves (with

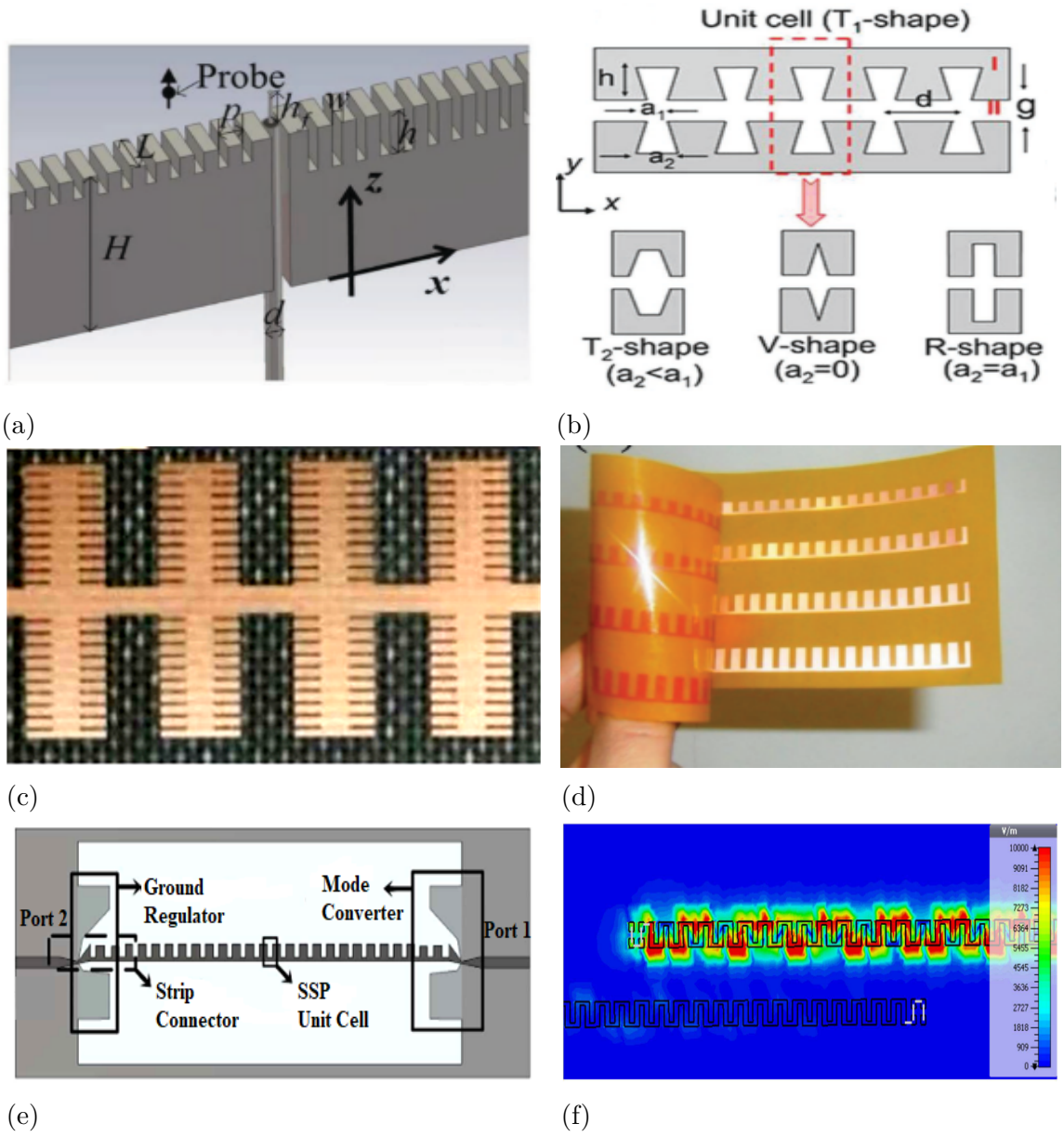

Figure 1.5: A set of spoof SPPs waveguides (a) the metallic grates that have a finite thickness (L) [33], (b) the complementary plasmonic waveguide with four different shapes of grooves [35], (c) the primary corrugated strips as slots aligned parallel to one another [39], (d) the conformal surface plasmons waveguide on a flexible dielectric film [34], (e) the SW-TL where SSP structure connected to the microstrip line [37], and (f) meander slow wave transmission line [38].

k_{spp}) will effectively transform into radiating waves (with k_0) as they approach and propagate down the 1-D metasurface. The horizontal wave vectors on the two interfaces must fulfill the following relation as given in [59] for the generalized Snell's law to apply:

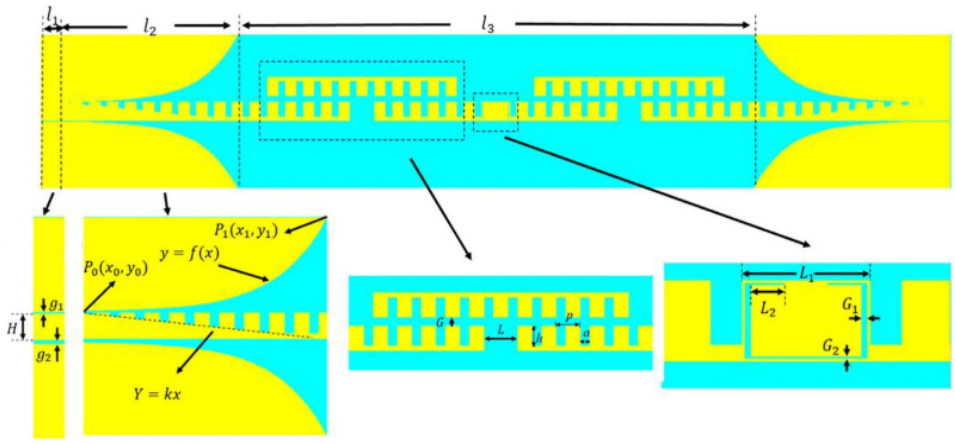

Figure 1.6: The broadband band-pass filter [45].

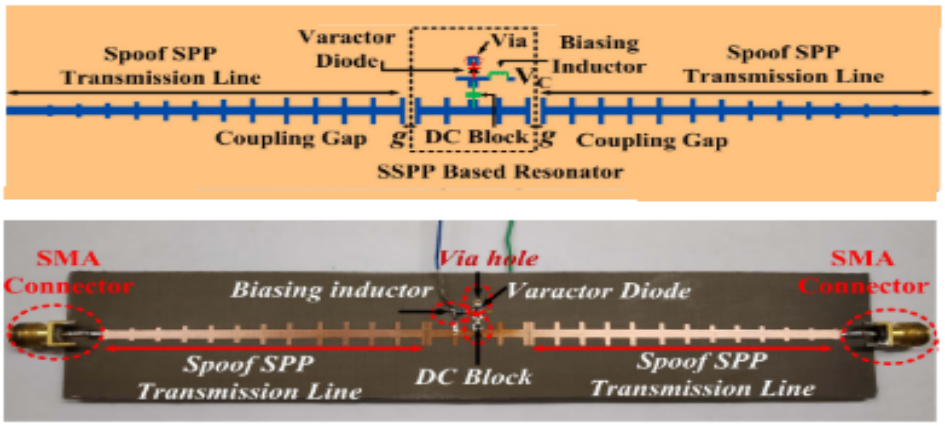

(a)

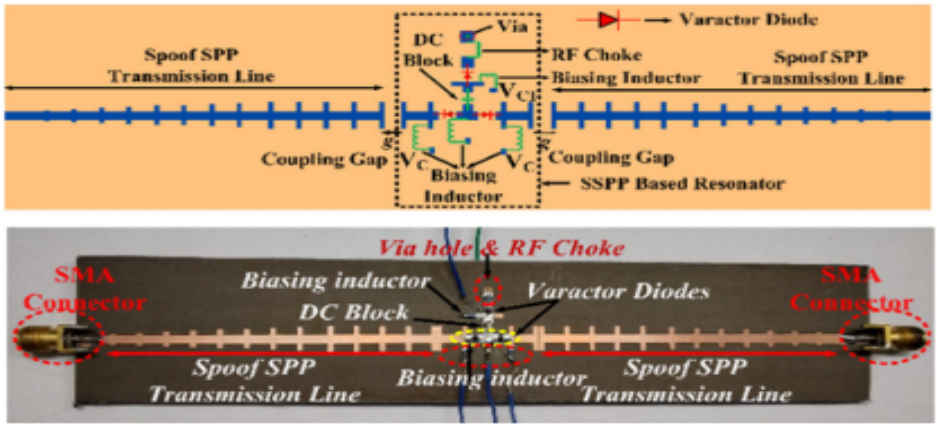

(b)

Figure 1.7: (a) a schematic and manufactured prototype of the bandwidth reconfigurable BPF based on a T-shaped SSPP resonator [44], and (b) a schematic and fabricated prototype of the spoof SPP-based varactor-loaded tunable filter [46].

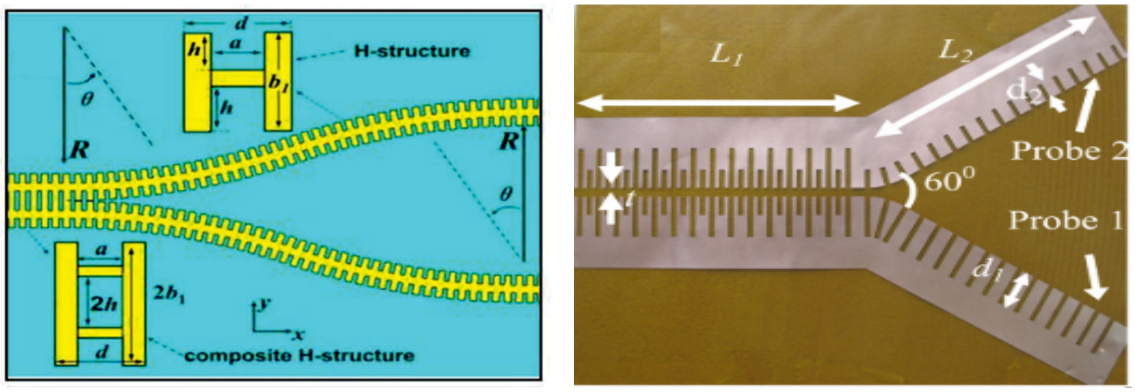

(a) (b)

Figure 1.8: (a) the plasmonic Y-splitter of H-shaped and composite H-shaped structure [47], and (b) the ultrathin frequency splitter in microwave frequencies [55].

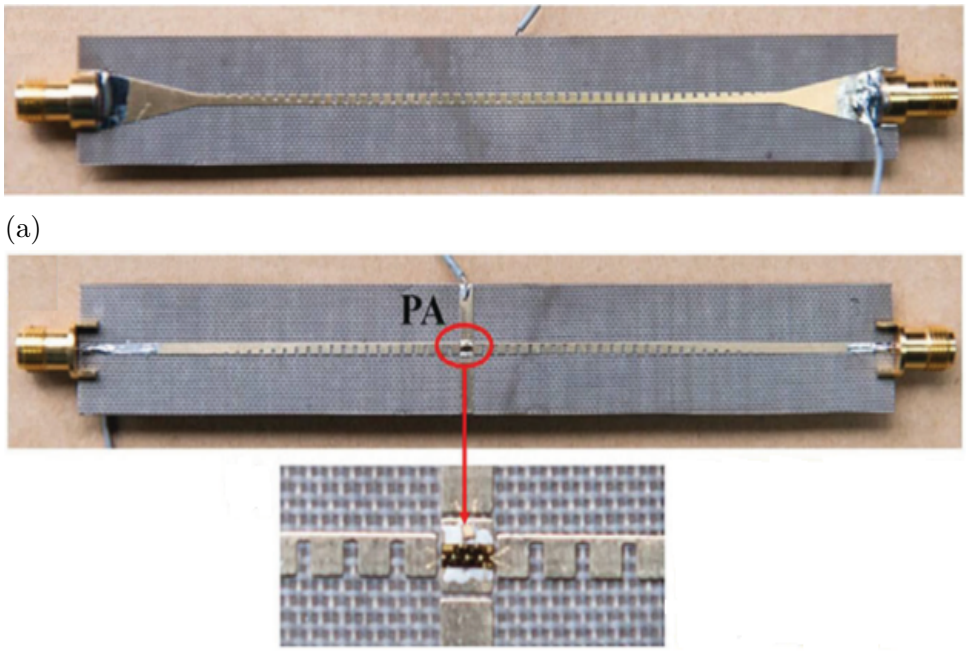

(a)

(b)

Figure 1.9: The manufactured prototype to amplify SSPPs (a) the rear view, and (b) the front view and its magnified perspective [56].

$$k_0 sin\theta_r - k_x sin\theta_i = \frac{d\Phi}{dx} \tag{1.11}$$

where k_x represents the SSPPs wave number and $\frac{d\Phi}{dx}$ is the the metasurface's phase discontinuity along the x-direction and θ_i and θ_r are the incident and reflected angles of the waves, respectively.

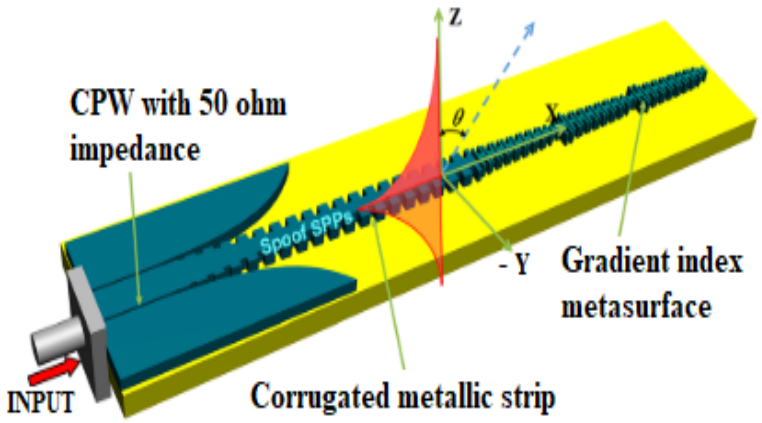

Figure 1.10: A broad view of the spoof SPP emitter [59].

1.4.1 SSPPs-based leaky wave antennas (LWAs)

A leaky-wave antenna (LWA) is a waveguiding structure with a mechanism that allows it to power leakage throughout its length. The general working principle of the leaky-wave antennas is discussed in [63]. LWAs are a class of antennas that use a traveling wave on a guiding structure as its primary source of radiation [64]. The first leaky-wave antenna was developed by Hansen in 1940 [65]. LWAs are frequency beam-scanning antennas with distinctive characteristics such as high gain and wide operating bandwidth. However, traditional LWAs are very bulky and complicated structures. Recently, there has been a notable growth in research and the pace of innovation related to planar LWAs. Planar LWAs includes microstrip line-based [66–68] and substrate integrated waveguide (SIW) based [69–74]. However, SIW based structures are intricate. Their efficiency was not as high due to the ground plane in the microstrip line and SIW-based leaky-wave antennas.

SSPPs-based antennas open a new era in the form of planar leaky-wave antennas. All of the characteristics of conventional LWAs, including backward-to-forward beam scanning, are supported by SSPPs-based LWAs, and the "open-stopband" trait of conventional LWAs can also be resolved. SSPPs belong to the general category of surface waves (non-radiating). The two best techniques for attaining the SSPPs line effective radiation are periodic modulation (discontinuities) and gradient pruning. In order to transform SSPPs into radiating waves, a periodically-modulated plasmonic

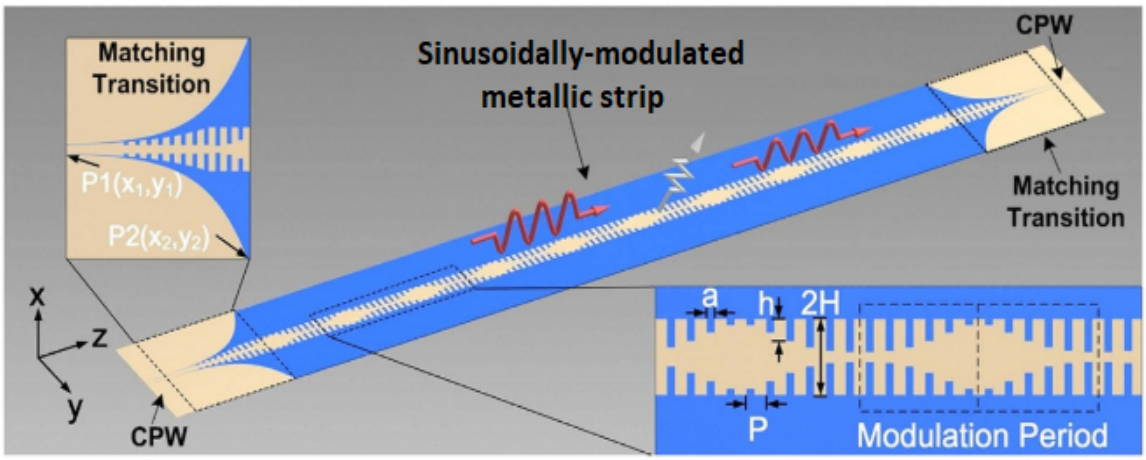

Figure 1.11: An illustration of a plasmonic waveguide with sinusoidal modulation utilizing a corrugated metal strip [60].

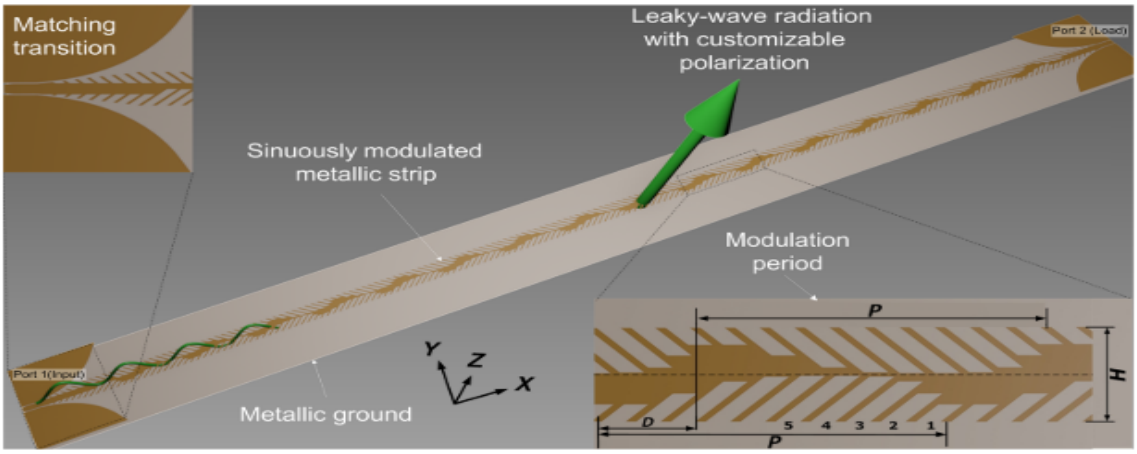

Figure 1.12: Schematic of the tilting unit-based LWA [75].

waveguide made of a non-uniform corrugated metallic strip was proposed in [60] as depicted in Fig. 1.11. An LWA with arbitrarily customizable polarizations was reported in [75], as shown in Fig. 1.12. The SSPP-based LWAs that use a proximity coupling mechanism were reported in many works [76–82]. A few of them are illustrated in Fig. 1.13.

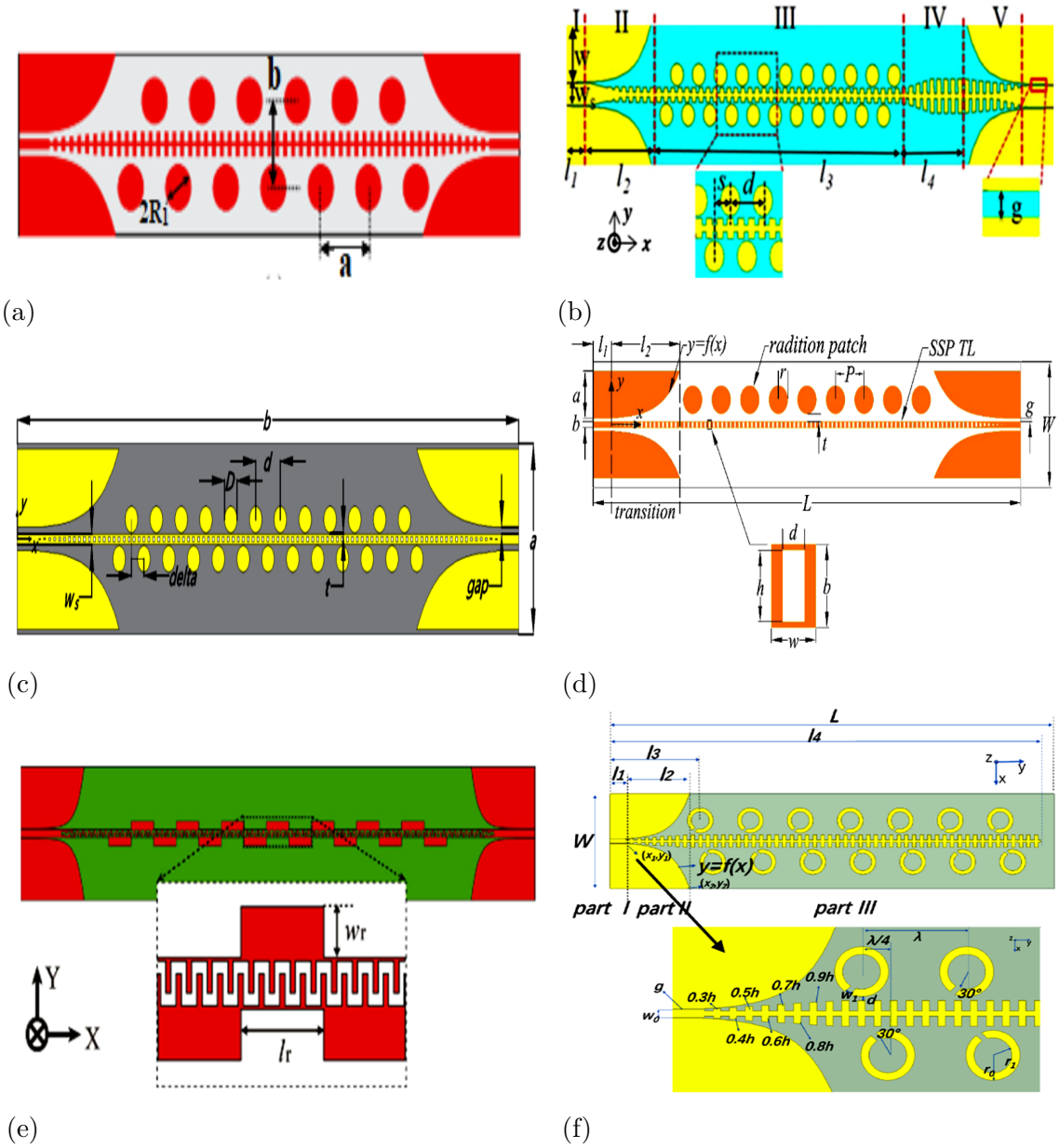

Figure 1.13: A set of SSPPs based LWAs (a) configuration of the periodically loaded patches based LWA [76], (b) a frequency-controlled beam-scanning antenna fed by the standing wave of SSPPs [77], (c) wide-angle beam scanning LWA [78], (d) single-beam LWA with lateral scanning [79], (e) continuous scanning LWA based on second-mode [80], and (f) broadband circularly polarized (CP) LWA [81]

.

1.4.2 SSPPs-based endfire antennas

The end-fire antennas are employed to transmit the power into free space along the direction of the antenna advancement. The primary direction of maximum radiation is parallel with the antenna design. End-fire antennas offer a superior low aerody-

namic drag profile for real-world applications, including radar, missiles, and aerial vehicles. Several types of endfire antennas, such as Yagi-Uda, tapered slot, leaky wave, and log-periodic, are reported in the literature. Endfire antennas have been the subject of numerous research studies [83–89]. Nevertheless, it might be challeng-

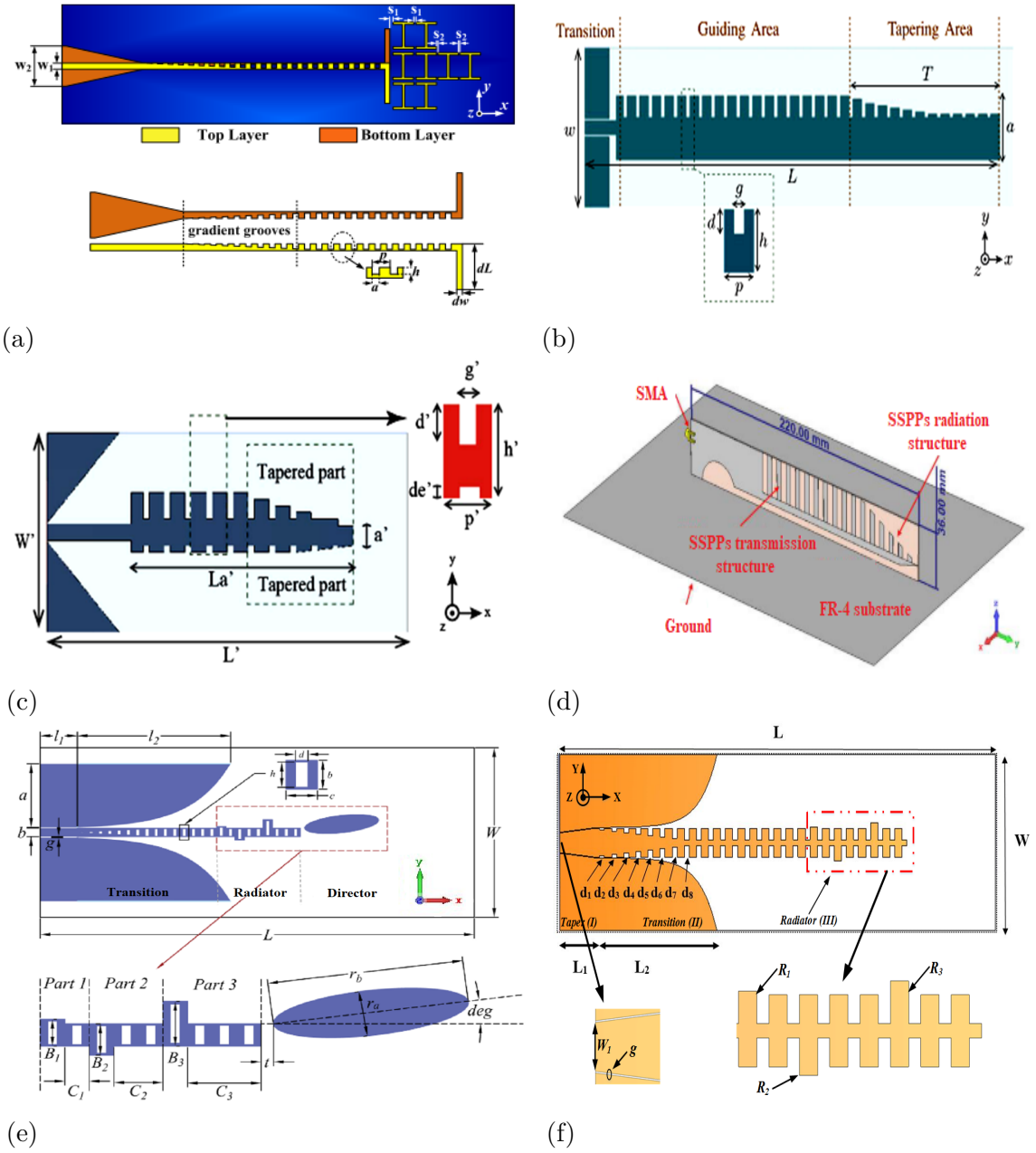

Figure 1.14: A set of SSPPs based endfire antennas (a) a metamaterial-based endfire antenna [83], (b) low-profile traveling wave endfire antenna [84], (c) broadband frequency scanning endfire antenna [85], (d) a vertically polarized endfire antenn [86], (e) a single layer high gain endfire antenna [87], and (f) a planar low-profile endfire antenna [88].

ing to implement a low-profile structure without losing effectiveness. A dipole-like SSPPs-fed antenna was developed in [83] for endfire radiation. However, due to the resonant nature of the dipole-like radiator, it is narrowband. After that, many traveling wave antennas were developed using the SSPPs structure, which exhibits wideband characteristics. A few of them are depicted in Fig. 1.14.

1.5 Multiple Input Multiple Output (MIMO) System Implementation using SSPPs-based Endfire Antennas

MIMO technology provides higher data rates by independently increasing the number of channels, which requires multiple antenna elements, *i.e.*, M at the transmitting (T_X) end and N at the receiving (R_X) end, as shown in Fig. 1.15. Therefore, an $M \times N$ number of independent data streams are set up between the transmitter and receiver channel modules by employing spatial multiplexing at the same operating frequency. Consequently, the wireless link's channel capacity and spectral efficiency increased without requiring more bandwidth or transmitted power. The invention of MIMO technology dates back to Winter's 1984 article [90]. Researchers later published some research papers and patents to further comprehend the MIMO system advancements [91–94]. However, incorporating multiple antenna elements in the

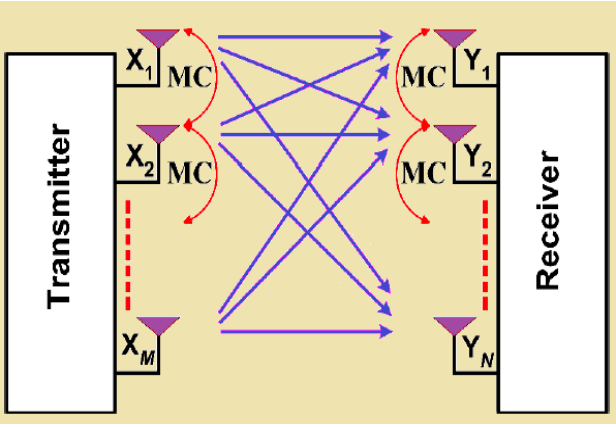

Figure 1.15: MIMO system with *(M × N)* antenna elements.

MIMO system is more challenging due to their strong mutual coupling. In the MIMO system, the EM wave interaction between antenna elements is known as mutual coupling, denoted as MC measured in dB. The value of S-parameters between the i^{th} and j^{th} element is given as $(10\log 10_{10}|s_{ij}|)$. The MIMO system configuration and element excitations are the determining factors. In this way, the EM wave is absorbed by one antenna when another one radiates. Consequently, their interaction tends to affect the antenna elements' radiation patterns, efficiency, reflection coefficient, and impedance-matching behavior. In [95], an empirical model of mutual coupling MC_{ij} was published.

$$MC_{ij} = exp(-\frac{2d_{ij}}{\lambda}(\alpha + n\pi)), i \neq j \tag{1.12}$$

$$MC_{ij} = 1 - \frac{1}{N}\sum_{i}\sum_{i \neq j} MC_{ij} \tag{1.13}$$

where the distance between i^{th} and j^{th} antenna elements is denoted by d_{ij}, α is controlling parameter for the coupling level, N is the total number of antenna elements in the system. Mutual coupling mechanisms in the transmitting and receiving modes are discussed in [96]. Mutual coupling in the conventional MIMO antenna system occurs due to three factors: space radiations, surface waves, and surface currents. The electromagnetic coupling (EMC) in the conventional two-antenna MIMO system in different topologies is beautifully explained in Fig. 1.16. Fig. 1.16 depicts all possible ways of MC in the MIMO system. As demonstrated in Fig. 1.16a, considerable EMC between antenna elements is found when situated closely on a single substrate with a shared ground plane. This is because of the high port-to-port coupling due to space, surface, and conducting waves. In the case of 1.16b, the effects of the conducting waves were eliminated by applying the concept of a partial ground plane; still, the scattered wave from the edges of the partial ground causes unwanted coupling. In Fig. 1.16c topology, the antennas are placed on the partial substrate with a common ground plane. As a result, coupling slightly reduces due to the absence of surface waves. However, scattered waves produce undesirable coupling. Finally, as shown in Fig. 1.16d, two distinct patch antennas are positioned at a certain distance. The

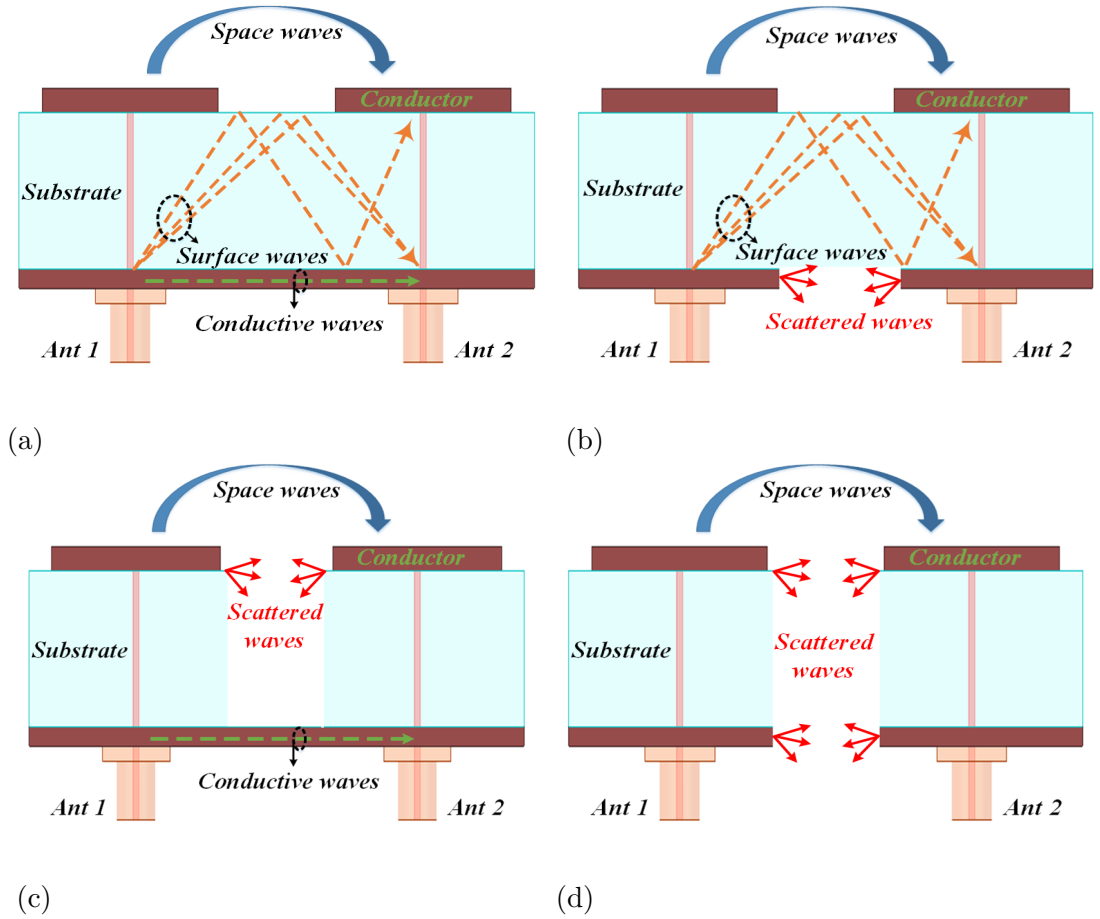

Figure 1.16: Electromagnetic coupling between two antennas (a) patches with common ground on the same substrate, (b) patches with partial ground on a distinct substrate, (c) patches on a partial substrate with common ground, and (d) separate antennas.

lowest EMC is seen in this arrangement due to the total dearth of conducting and surface waves.

The conventional MIMO system either required appropriate separation between the antenna elements or required some additional structures to achieve better isolation and focused end-fire radiation, like electromagnetic band-gap (EBG) structures, metasurface (MS), directors, and reflectors, which complicates the design. The SSPPs based endfire antenna introduces a novel concept for achieving high isolation and high signal integrity in the MIMO antenna system without using any decoupling structure. Endfire antennas using SSPPs-based TL accomplish this due to their excellent field confinement ability. Moreover, the SSPPs-based structures can concentrate electromagnetic (EM) waves into subwavelength scales, which is a boon in miniaturizing the

advanced circuits and systems [97].

1.5.1 The MIMO system performance metrics

To estimate the correct behavior of the MIMO antenna system in a practical scenario. The study of several performance metrics is a necessary, such as isolation (coupling), envelope correlation coefficient (ECC) by the S-parameters and 3-D field [98], total active reflection coefficient (TARC) [99], and channel capacity loss (CCL) [100], which are discussed in the following section.

Envelope correlation coefficient (ECC)

The envelope correlation coefficient (ECC) quantified the isolation or correlation amount among antenna elements. This metric considers the antenna system's radiation pattern and the degree to which the patterns interact when used simultaneously. A lower value of ECC denotes better pattern variety. In the N-element MIMO antenna, the ECC can be computed between the i^{th} and j^{th} elements using two different techniques: the S-parameters and 3-D field complex field equations [98], that is,

$$ECC = \rho_e(i,j,N) = \frac{|\sum_{n=1}^{N} S_{i,n}^{*} S_{n,j}|^2}{\Pi_{k=i,j}[1-\sum_{n=1}^{N} S_{k,n}^{*} S_{n,k}]} \tag{1.14}$$

$$ECC = \rho_e(i,j,N) = \frac{|\iint_{4\pi}[\vec{F}_i(\theta,\phi) * \vec{F}_j(\theta,\phi)]d\Omega|^2}{\iint_{4\pi}|\vec{F}_i(\theta,\phi)|^2 \iint_{4\pi}|\vec{F}_j(\theta,\phi)|^2} \tag{1.15}$$

where $F_i(\theta,\phi)$ and $F_j(\theta,\pi)$ are 3-D complex field patterns of i^{th} and j^{th} antenna elements in the N-elements MIMO system, respectively. For the practical MIMO system in the fading environment, the ECC value must be smaller than 0.5 [101].

Total Active Reflection Coefficient (TARC)

The MIMO system cannot be adequately characterized using the scattering matrix alone. Therefore, a generalized parameter known as the total active reflection coefficient (TARC) is introduced to analyze the multiport MIMO system properly. For

the multiport MIMO system, the TARC is the ratio of the square root of the total reflected power and the square root of the total incident power. The TARC of the N-element MIMO system is estimated using the scattering matrix given [99] by

$$\Gamma_a^t = \frac{\sqrt{\sum_{n=1}^{N} |b_i|^2}}{\sqrt{\sum_{n=1}^{N} |a_i|^2}} \tag{1.16}$$

In a multi-port network with comparable characteristic impedances at each port, it can be calculated using the S parameters, given as

$$\mathbf{b} = \mathbf{sa} \tag{1.17}$$

where s is the scattering matrix, b_i is the reflected signal, and a_i is the incident signal. In addition to coupling, the TARC also considers random-signal combinations between ports. The value of the TARC ranges from 0 to 1, where 0 indicates the radiation of all incident power and 1 denotes that there was no radiation and all incident power was reflected. The S-parameter matrix for a 3-port MIMO system will be 3 × 3.

$$\begin{bmatrix} b_1 \\ b_2 \\ b_3 \end{bmatrix} = \begin{bmatrix} S_{11} & S_{12} & S_{13} \\ S_{21} & S_{22} & S_{23} \\ S_{31} & S_{32} & S_{33} \end{bmatrix} \times \begin{bmatrix} a_1 \\ a_2 \\ a_3 \end{bmatrix} \tag{1.18}$$

Moreover, the influence of a feeding phase on the antenna port is also included in the TARC. The TARC (Γ_a^t) for a 3-elements MIMO system can be calculated using the given [99] equation,

$$\Gamma_a^t = \frac{\sqrt{(|S_{11} + S_{12}\exp^{j}\theta_2 + S_{13}\exp^{j}\theta_3|^2) + (|S_{21} + S_{22}\exp^{j}\theta_2 + S_{23}\exp^{j}\theta_3|^2) + (|S_{31} + S_{32}\exp^{j}\theta_2 + S_{33}\exp^{j}\theta_3|^2)}}{\sqrt{2}} \tag{1.19}$$

so, to estimate the TARC realistically, antenna elements are excited at unity amplitude with varying phases from 0° to 360°. Three cases are considered to excite the antenna elements: Case_1: 1 = 0°, 2 = 90°, 3 = 180°; Case_2: 1 = 0°, 2 = 180°, 3 = 270°; and Case_3: 1 = 0°, 2 = 270°, 3 = 360°, where 1, 2, and 3 are Ant 1, 2, and 3, respectively

Channel Capacity Loss (CCL)

The channel capacity can be enhanced by expanding its antenna array in a MIMO system. However, channel capacity loss will occur from uncorrelated Rayleigh fading in MIMO channels. The CCL is estimated by using eq. given [100] below,

$$C_{loss} = -\log_2 \det(\psi^R) \tag{1.20}$$

where $\psi^R = [\rho_{ij}]$ represents the receiving antenna's correlation matrix, given as, ρ_{ii} $= 1 - |\sum_{n=1}^{N} S_{in}^{*} S_{ni}|$ and $\rho_{ij} = -|\sum_{n=1}^{N} S_{in}^{*} S_{nj}|$ for (i,j), $(i \neq j) \in (1, 2, 3....N)$. It is imperative to assess the efficacy of MIMO antenna performance using the performance metrics specified above.

1.6 Reflectarray System Design using SSPPs-based Endfire MIMO feed

A reflectarray is composed of an array of radiating elements that provide a pre-adjusted phasing to generate a collimated beam when it is powered by a feed, similar to a parabolic antenna [102]. The idea of reflectarray antennas was first invented by the Berry *et al.* in the 1963, utilizing short-terminated variable-length waveguide [103]. Fig. 1.17 depicts the experimental prototype of the waveguide reflectarray. Although this initial reflectarray antenna's design was quite innovative, a major problem was its heavy and massive waveguide structure. So, Malagisi introduced the new concept of RA antenna design on a planar structure in the 1980s, as discussed in [104]. Recently, metallic planar structures stimulated with a spatial feed mechanism for long-distance communications and radar applications are trending. It has the characteristics of a reflector and array known as a reflectarray (RA), with notable advantages such as being lightweight, low profile, high gain, and possessing minimal levels of cross-polarization. Fig. 1.18 shows a typical model of a reflectarray antenna. Each element is engineered to integrate a specific reflected phase when it

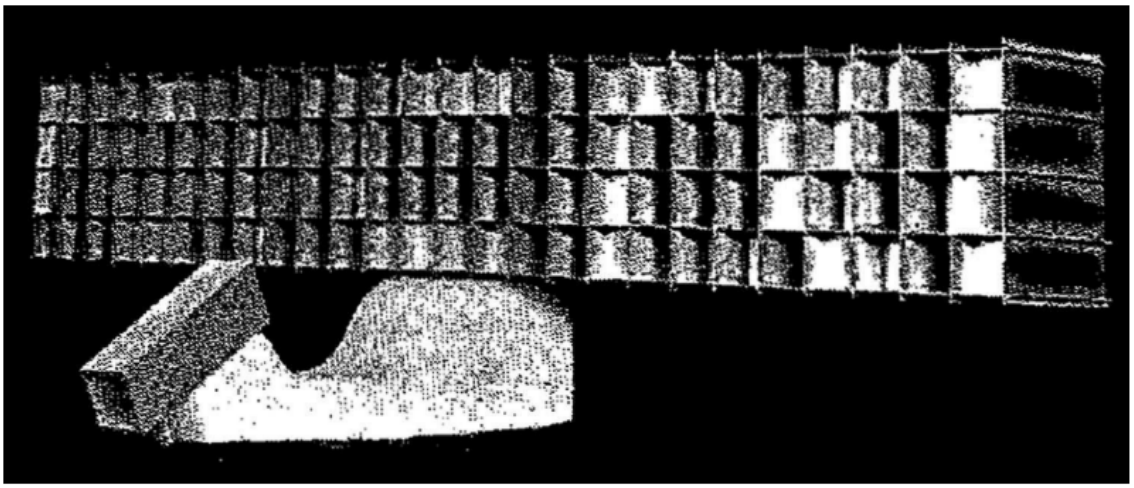

Figure 1.17: The experimental setup of the first waveguide-based reflectarray [103].

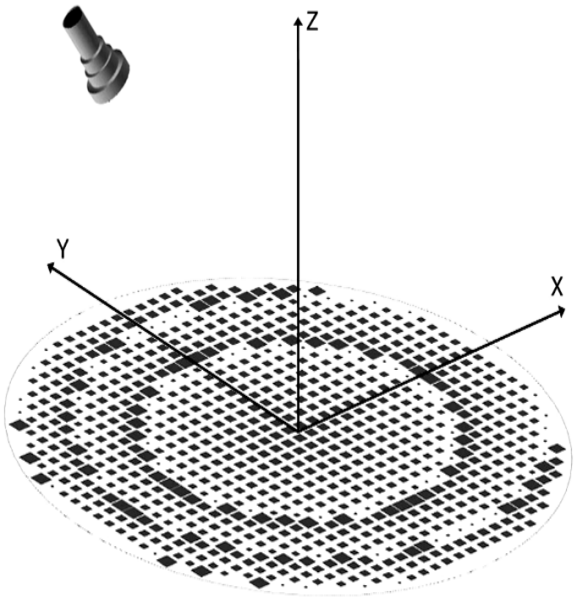

Figure 1.18: The basic architecture of a planar reflectarray antenna [105].

gets illumination from the feed antenna. The next step is to synthesize the phase distribution throughout the reflectarray aperture, which enables the reflectarray to produce a shaped or collimated beam in the specified direction.

1.6.1 The operational principle

A reflectarray's primary function is to focus an incoming uncollimated electromagnetics wave into a directed planar wave. Reflectarrays, unlike parabolic reflectors, do

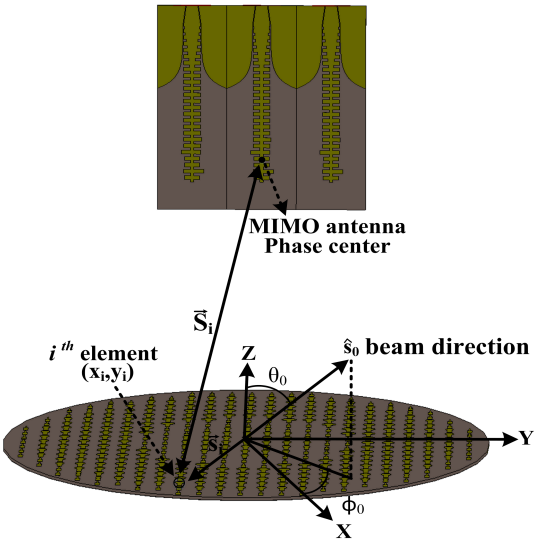

Figure 1.19: MIMO feed reflectarray configuration.

not require physical curvature to achieve the spatial compensation of the incoming wave's phase. The fundamental working principle of the proposed RA antenna is demonstrated in Fig. 1.19. The EM waves are transmitted through the feed antenna and reflected by the reflector. This introduces the spatial phase delay (spd) between the feed antenna phase center and that element. The reflectarray element's reflection phase should restitute for the spd (ϕ_{spd} = -$k_0 \cdot S_i$), where k_0 is the wave vector in the free space, and S_i is the separation between the feed antenna phase center and the i^{th} element. The output high-gain beams of the RA come along broadside direction (θ_0,ϕ_0), which can be focused in any desired direction by incorporating a successive phase (ϕ_{sp} = -$k_0 \cdot \vec{s}_i \cdot \hat{s_0}$) to the aperture. The element position on the RA surface is (x_i, y_i) can be presented in a spherical direction (θ_0, ϕ_0) and successive phases, given as,

$$\phi_{sp} = -k_0(x_i \sin\theta_0 \cos\phi_0 + y_i \sin\theta_0 \sin\phi_0) \tag{1.21}$$

therefore, the desired phase shift on the reflectarray aperture (ϕ_{RA}), must incorporate the successive phase and the spatial delay (spd). *i.e.*

$$\phi_{RA} = \phi_{spd} + \phi_{sp} \tag{1.22}$$

$$\phi_{RA} = k_0(S_i - (x_i \cos\phi_0 + y_i sin\phi_0)\sin\theta_0) \tag{1.23}$$

the above expression of the desideratum phase will produce the converged beam in the specified direction.

1.6.2 Methods of phase tuning

The choice of a phase-tuning approach is a crucial step in the reflectarray design. It permits the appropriate phase tuning range to be achieved by the reflectarray elements. There are various methods for shifting the phase of reflectarray elements, broadly divided into three categories, as depicted in Fig. 1.20: elements featuring phase/time delay lines, varied sizes, and variable rotation angles [105].

Elements featuring phase/time delay lines

In this technique, the patch element receives the electromagnetic waves from the feed antenna and transforms them into a guided wave that travels along a transmission line (usually a microstrip line) of a specific length. Two ways to terminate a transmission line are open and short circuits, as shown in Fig. 1.20a. The element reradiates the signal after reflecting from the transmission line termination. According to this technique, the phase shift is equal to two times the line length, which is determined by

$$\phi_{delayline} = 2kl \tag{1.24}$$

where k is the signal's propagation constant, and l is the line's length.

Variable-sized elements

In this technique, phase adjustment is accomplished by altering the element's physical size, as depicted in Fig. 1.20b. It is well known, theoretically, that changing a resonant element's length alters the antenna's resonance frequency, which also changes the radiated phase at a particular frequency. Therefore, the idea behind the variable-size approach is that resonant patches of varying sizes will produce different reflected phases. The variable element size technique was initially reported for printed crossed dipoles in [106], for rectangular shaped patches in [107], and for square or circular patch geometry in [108].

Elements with varied rotation angles

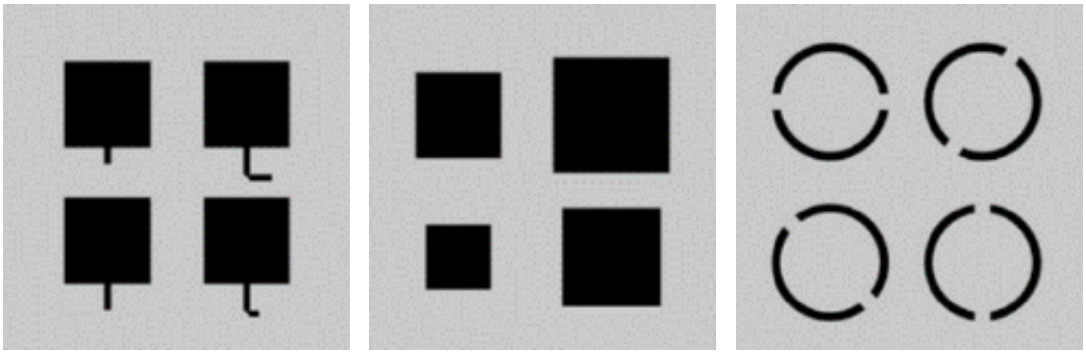

(a) (b) (c)

Figure 1.20: Phase tuning approaches for reflectarray (a) patches with varying lengths of phase delay lines, (b) patches of varied sizes, and (c) split rings with different degrees of rotation.

The basic concept of this approach is that the rotation of a CP antenna element by ψ° around its origin will result in an equal change in the radiated phase, where the rotational direction determines whether the phase advances or is delayed, as shown in Fig. 1.20c. Initially, patches with varying lengths of phase delay lines were used to apply this approach to reflectarrays [109]. The reflected wave experienced a phase shift that is a linear function of the rotation angle when the patches were turned around the unit cell's center or their origin.

1.6.3 Beam scanning reflectarray

Traditionally, reflector (or lens) antennas and phased array antennas were used to achieve high-gain beam scanning. Reflector antennas require a mechanical approach or through an intricate feed cluster, while phased array requires phase shifter technology which needs a large hardware layout and is expensive [110–113]. RA is also beneficial in various beam scanning applications where stable communication is desired, such as mobile vehicles and dense building areas. In [114], Nayeri *et al.* categorized the beam-scanning RA antenna techniques as aperture phase-tuning and feed-tuning. Feed tuning can be achieved through movable feed of single antenna or by multiple feed arrays system. In the aperture phase tuning, the RA elements on the aperture surface are configured with a phase-tuning technique or by various enabling technolo-

gies. The MIMO feed RA antenna is capable of generating multi-beams to provide a stable communication.

In order to stimulate the RA, mitigate the aperture blockage, and achieve continuous beam scanning without geometrical intricacy, the SSPPs-based endfire MIMO antenna is an appealing choice. The SSPPs-based antenna structures are trending nowadays because of their attractive features, such as low profile, low mutual coupling, high signal integrity, and subwavelength field confinement. The low profile and coplanar geometry overcome the aperture blockage. The subwavelength field confinement ability is advantageous for miniaturizing complex circuits and systems [97].

1.7 Motivation

In the current research scenario, SPP-based devices and circuits are trending because of their attractive features, such as miniaturization, interference suppression, low profile, less complexity, high signal integrity, and subwavelength confinement ability. The first significant step toward developing SSPs-based devices was after the invention of highly efficient interfaces connecting SSPs to traditional microwave TLs. The prime motivation of this thesis is to thoroughly investigate the aforementioned traits through the design of the LWA and endfire MIMO antennas. In the existing literature, most of the reported planar SSPPs leaky-wave antennas have longer physical lengths with matched terminations. So, a compact-size, high-gain, low-profile single-port leaky-wave antenna is designed. One of the primary challenges in developing a MIMO system is to ensure low mutual coupling between antenna elements. The conventional coupling reduction techniques are studied, and challenging factors are identified. However, some techniques increase the complexity of the implementation. So, the motivation is to unleash a novel method that minimizes mutual coupling and improves MIMO performances without adding geometrical intricacy. Endfire MIMO antenna using SSPPs-based TL accomplishes this due to their excellent field confinement ability. The reflectarray was illuminated in existing literature using antennas

such as the E-plane, H-plane, conical, and pyramidal horn antennas. Implementing these horn antennas as a feed element introduces blockages of some reradiated power due to their large aperture size. Reduced gain and increased side lobe level are the main consequences of aperture blockage. In addition to fixed beam applications, RA is also beneficial in various beam scanning applications where stable communication is desired. So, the endfire MIMO antenna as a feeding element for RA has a very high isolation property due to its high field confinement ability, making it suitable for continuous beam scanning. Its low profile and coplanar geometry overcome the aperture blockage.

1.8 Organization of this Thesis

This thesis is organized into the following five chapters:

Chapter 1 begins with the background of natural surface plasmon polaritons (SPPs) and spoof surface plasmon polaritons (SSPPs) and discussed their fundamental characteristics and applications. Further, different SSPPs devices, including SSPP waveguides, filters, couplers, power splitters, and antennas, are also discussed. Furthermore, the MIMO system and Reflectarray system design brief history, challenges, performance characteristics, and operational principles are also discussed. Finally, the motivation and structure of this thesis are discussed.

Chapter 2 presents the realization of a single-port leaky-wave antenna powered by a spoof surface plasmon polaritons (SSPPs)-based line, which has a high gain, a low profile, and a compact size. It is implemented using a variable-width strip dipole. The designed antenna is intended to be used as a low-profile antenna for radar and wireless communications.

Chapter 3 focuses on the design, modeling, and analysis of a three-element, low-profile, coplanar endfire multiple-input-multiple-output (MIMO) antenna based on spoof surface plasmon polaritons (SSPPs). It achieves high isolation without any decoupling structure. The proposed MIMO antenna exploits the inherent feature of

high isolation in the SSPPs TL due to its strong field confinement competency. The proposed antenna is appropriate for X-band vehicular radar applications.

Chapter 4 introduces the realization of an X-band Beam-Scanning Reflectarray (RA) fed by a spoof surface plasmon polaritons (SSPPs)-based endfire MIMO antenna. The RA is based on a variable, elliptical-shaped unit cell. The SSPPs-based low-profile endfire MIMO antenna mitigates the aperture blockage, achieves high isolation between the feed elements, and accomplishes continuous one-dimensional (1-D) beam scanning. The proposed RA benefits nano-satellite applications.

Chapter 5 finally summarizes the concluding remarks and the previous chapters' investigations. This chapter also emphasizes the future potential of the presented research.

Fig. 1.21 shows the thesis's organizational framework.

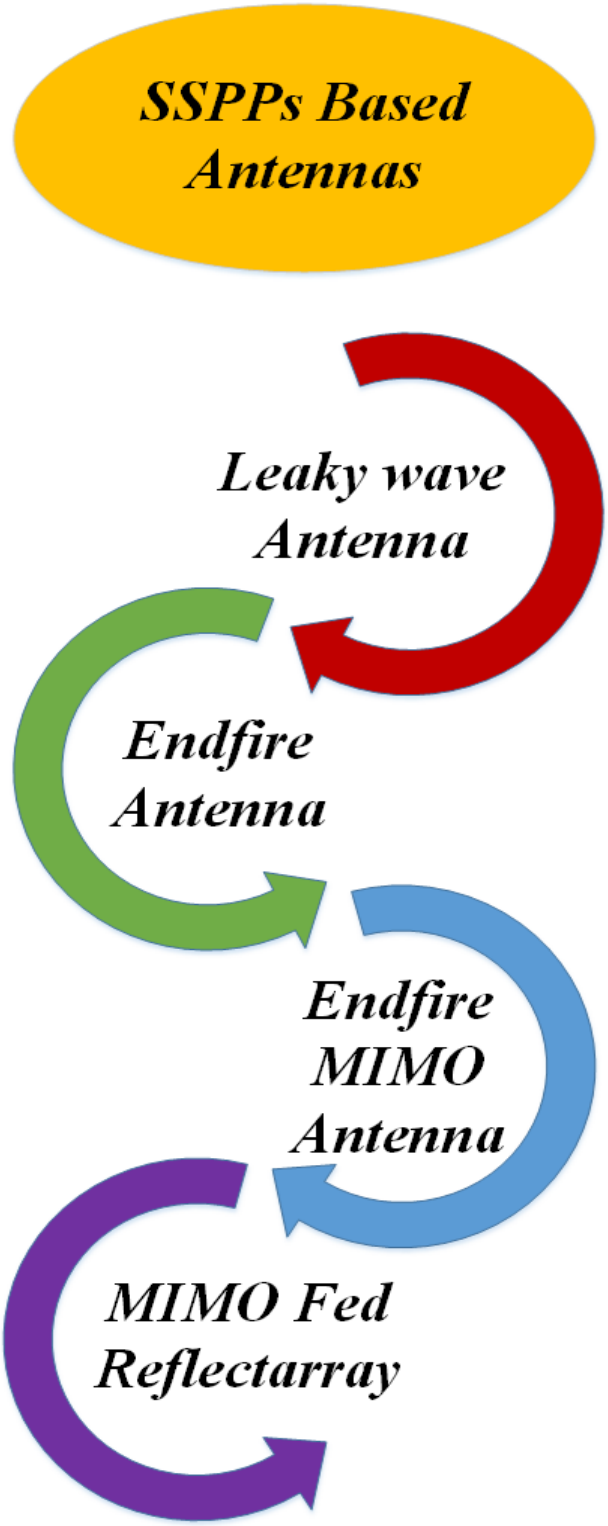

Figure 1.21: Organization of thesis work.